

Self-Aligned Single-Electrode Actuation of Tangential and Wineglass Modes using PMN-PT

Ozan Erturk¹, Kilian Shambaugh², Ha-Seong Park³, Sang-Goo Lee³, Sunil A. Bhave^{1,†}

¹*OxideMEMS Lab, Purdue University, West Lafayette, IN, USA*

²*Polytec Inc., Irvine, CA, USA*

³*iBULe Photonics Company Ltd., Incheon 21999, South Korea*

[†]*E-mail: bhave@purdue.edu*

Abstract:

Considering evolution of rotation sensing and timing applications realized in Micro-electro-mechanical systems (MEMS), flexural mode resonant shapes are outperformed by bulk acoustic wave (BAW) counterparts by achieving higher frequencies with both electrostatic and piezoelectric transduction. Within the 1-30 MHz range, which hosts BAW gyroscopes and timing references, piezoelectric and electrostatic MEMS have similar transduction efficiency. Although, when designed intelligently, electrostatic transduction allows self-alignment between electrodes and the resonator for various BAW modes, misalignment is inevitable regarding piezoelectric transduction of BAW modes that require electrode patterning. In this paper transverse piezoelectric actuation of [011] oriented single crystal lead magnesium niobate-lead titanate (PMN-PT) thin film disks is shown to excite the tangential mode and family of elliptical compound resonant modes, utilizing a self-aligned and unpatterned electrode that spans the entire disk surface. The resonant mode coupling is achieved employing a unique property of [011] PMN-PT, where the in-plane piezoelectric coefficients have opposite sign. Fabricating 1-port disk transducers, RF reflection measurements are performed that demonstrate the compound mode family shapes in 1-30 MHz range. Independent verification of mode transduction is achieved using in-plane displacement measurements with Polytec's Laser Doppler Vibrometer (LDV). While tangential mode achieves 40°/sec dithering rate at 335 kHz resonant frequency, the n=2 wine-glass mode achieves 11.46 nm tip displacement at

8.42 MHz resonant frequency on a radius of 60 μm disk resonator in air. A single electrode resonator that can excite both tangential and wine-glass modes with such metrics lays the foundation for a BAW MEMS gyroscope with a built-in primary calibration stage.

1 Introduction

Contour-mode bulk acoustic wave resonators have gained attention in the past decade due to their ability to beat the limitations of flexural mode resonators (such as low Q and low resonance frequency) for various application domains from RF filters to gyroscopes. Considering disk structures, displacement profiles of all contour vibrations of circular plates have been reported¹ (a correction to frequency equation to $n = 2$ wine-glass mode is published in a later work²), where modes of vibrations are classified into two parts when circumferential order n is equal to 0: namely radial mode (absence of rotation) and tangential mode (absence of areal dilation). The higher order in-plane compound modes ($n > 1$) incorporate both tangential and areal dilation at the same time. In conventional piezoelectric MEMS materials such as aluminium nitride (AlN), or lead zirconium titanate (PZT), when a disk resonator is designed with unpatterned electrodes as shown in Figure 1a, it is only possible to excite radial modes due to the strain coupling caused by the in-plane piezoelectric coefficients having the same sign. When more complex compound modes are desired for various applications, designers have to employ segmented electrodes in order to match the piezoelectrically generated strain profile to the intended contour mode of vibration and avoid charge cancellation^{1,3-5}. Figure 1b shows a schematic representation of such segmented electrode configuration that is necessary to transduce $n = 2$ compound mode (wine-glass mode) as an example. This family of compound modes ($n > 1$) have been demonstrated to be useful in RF filters^{6,7} and gyroscopes⁸⁻¹⁰. However, use of segmented electrodes for mode shapes of importance such as wine-glass modes inevitably causes misalignment in piezoelectric transduction topology due to patterning of top electrodes that require a separate lithographic step during fabrication. Misalignment of the electrodes causes excitation of spurious modes that are in close proximity to the mode of interest in the frequency domain or cause undesired out-of-plane components⁶. Self-alignment is possible in electrostatic actuation of compound modes since the same structural layer is used

to realize electrodes and the resonant body^{9,11}. It is not possible to achieve self-alignment in the piezoelectric domain to realize any resonant mode other than the radial mode depicted in Figure 1b. Therefore, even if piezoelectric transduction is accepted to provide more robust integration and efficient coupling compared to electrostatic transduction of BAW modes, in recent works it has been reported that microfabrication advancements allowed comparable performance of BAW gyroscopes and timing references for electrostatically actuated BAW modes^{9,12-15}. As electrostatic transduction is achieved through normal forces, shear displacement required to achieve tangential mode is not possible to excite using electrostatics. Moreover, tangential mode cannot be excited with traditional piezoelectric materials because their in-plane piezoelectric coefficients have the same sign^{1,5,16}. Therefore, there has been no demonstration of a tangential mode or compound modes using a single unpatterned electrode.

In this paper, we demonstrate efficient transduction of compound modes as well as the tangential mode in a piezoelectric disk resonator by a single self-aligned electrode utilizing the in-plane anisotropy of [011] lead magnesium niobate-lead titanate (PMN-PT). We extensively report on transduction of $n = 2$ wine-glass mode (WGM) because it is of particular interest for gyroscopy. In addition, we measure and optically verify the tangential mode transduction. The tangential mode is isochoric with no out-of-plane-displacement, which is an attractive feature for MEMS clocks, resonant sensors, and an integrated calibration stage for gyroscopes.

2 Results

Lead magnesium niobate-lead titanate (PMN-PT) PMN-PT is a relaxor type ferroelectric material, discovered in 1997. It quickly became popular in various applications due to its superior piezoelectric constant and high coupling coefficient values as well as its ability to be grown in single crystal form^{17,18}. [011]_c single crystal PMN-PT is reported to have opposite polarity of the in-plane piezoelectric coefficients¹⁹, namely d_{31} and d_{32} as shown in Figure 1. This unique property is utilized to rotate magnetic domains in multiferroic structures, taking advantage of the compressive stress along one direction and tensile stress along the orthogonal in-plane direction^{20,21}.

Correspondingly, WGM shape is realized without the need for segmented electrodes (as shown in Figure 1c) since PMN-PT produces in-plane strain that has opposite direction in x- and y-axes under transverse electric field, hence enforcing wine-glass mode shape naturally. Although not as intuitive, the unpatterned electrode can excite the tangential mode on the same disk structure (as depicted in Figure 1f) as well as higher order $n=3$ WGM shape.

In order to investigate the transverse actuation of modes of interest and their operation of frequency, finite element analysis (FEA) modeling of the disk resonators is performed using the COMSOL piezoelectric module. Adopting the material properties of [011] PMN-PT with d_{31} and d_{32} opposite signs¹⁹, a simplified COMSOL model with side tethers is implemented. This model calculates the mode shapes as shown in Figure 1f-h, and resonant frequencies of disk resonators with various radii ranging from $20\ \mu\text{m}$ to $75\ \mu\text{m}$, where resonant frequencies as a function of disk radius are plotted in Figure 3b.

Single-crystal PMN-PT film samples with $6\ \mu\text{m}$ -thickness developed by iBule Photonics are bonded to silicon carrier wafers as schematically shown in Figure 2a. While most bonding and fabrication process steps are identical to typical single-crystal Piezo-on-Insulator (POI) resonator fabrication, the most notable differences are in Figure 2c and d. A larger than required metal top electrode is patterned, in Figure 2c. Then the disk resonator body is defined and patterned smaller than the top metal to achieve self-alignment of the top electrode to the disk using CHISEL (CHanging Incident beam-angle for Sidewall Etching and Lapping, Supplementary Note 1). An SEM image of the completed etch step is shown in Figure 2h with annotated layers. Finally, exposed silicon is sacrificially etched using XeF_2 resulting in the self-aligned electrode resonator Figure 2e. An SEM image of the released disk resonator is shown in Figure 2g.

Device Design and Characterization Considering the most important geometric factor that determines the resonant frequency, namely radius of the disk, we designed disk resonators that have resonance frequency around 10MHz for wine-glass mode with radii (r_d in Figure 2g) ranging from $20\ \mu\text{m}$ to $75\ \mu\text{m}$. Given the material properties and analytical equations provided¹ (a correction to $n=2$ wine-glass mode family frequency equations is provided²), estimations of radius values

necessary to obtain WGM in the 1-30 MHz are determined and verified by FEA analysis. Side tethers are designed to decrease mechanical loss by choosing the lengths of the tethers (l_t in Figure 2g) to match the the quarter wavelength of $n=2$ WGM of varying radii. The width of the tethers (w_t in Figure 2g) are chosen to be as narrow as possible allowed by the critical dimension of the lithography^{2,22}.

Electrical RF reflection (S_{11}) measurements are performed on fabricated 1-port devices in air after the release step using Ground-Signal-Ground (GSG) pads as schematically shown in Figure 2g. Figure 3a shows the RF response of disk resonators with radii values ranging from $20\mu m$ to $75\mu m$. It is shown that although some spurious modes exist for some radii values, the most prominent resonant shape in the range of interest is the desired WGM. A comparison of the resonant frequencies for different radii resonators is shown in Figure 3b. For larger radii, the agreement between calculated and experimental data is greater due to influence of the side tethers getting less significant compared to the resonant body size.

We perform an independent verification of the mode shapes using a Laser Doppler Vibrometer (LDV). LDV videos of the tangential mode and $n=2,3$ WGM are provided in supplementary material (Supplementary Video 1,2, and 3 respectively). Cartesian grids (as opposed to polar distribution of data points) are employed for scanning the top surface of the resonators in order to establish equal spacing between data points and eliminate any possible spatial aliasing and geometrical biasing of the circular scanned space. Snapshots of the measured WGM are shown in Figure 4a at different phases of one cycle of oscillation for a disk resonator with radius of $60\mu m$ at 8.42 MHz. LDV measurement and data acquisition technique is described in detail in supplementary information (Supplementary Note 2).

We record the Y-displacement at two locations on the disk for the $n=2$ WGM. At Location-2, (denoted with a red-circle) which is the edge of the disk we measured a displacement of 11.46 nm in the Y-direction for an excitation amplitude of 1V as shown in Figure 4b, which is a comparable value to that of electrostatically transduced BAW gyroscopes. Since complete mapping of each disk resonator takes about 50 minutes, the LDV measurement grid may drift with respect to

the resonator over multiple scans. Therefore, in order to measure linearity, we chose Location-2 (denoted with the black-circle) that resides slightly towards the center to achieve a more stable measurement point as depicted in Figure 4a. The measured Y-displacement at this location shows linear displacement with applied voltage amplitude for the WGM.

We also measured the tangential mode using LDV. Snapshots of a single oscillation cycle is provided in Figure 5a for the same $60\mu m$ radius device. Since LDV measures in-plane displacement in X- and Y- directions, we calculated the angular displacement along a radial line with an average displacement of $19\mu^\circ$ at 335 kHz, which is the resonant frequency of the tangential mode for a disk with $r = 60\mu m$ radius. This corresponds to a rotation rate of $40^\circ/s$ when a 1V amplitude excitation signal is applied. In Figure 5b, the rate data is recorded for different voltage amplitude values showing a linear dependency of the rotation rate on the applied signal.

3 Discussion

We achieved transverse actuation of tangential and compound mode family resonant shapes on a piezoelectric disk resonator using a self-aligned single-electrode exploiting the unique in-plane anisotropy of [011] oriented single crystal PMN-PT. We developed a wafer-scale fabrication procedure involving a combination of wet etching and ion milling of PMN-PT films that is thickness non-uniformity tolerant and capable of producing a vertical side-wall profile with CHISEL technique. Considering gyroscope applications of the $n=2$ WGM, tip displacement of 11.46 nm is measured in LDV with 1V amplitude actuation signal. The self-aligned feature of this actuator can be attractive for quadrature-error free gyroscopes²³, tangential-mode TED-free oscillators. It is also important that obtained rotation rate values of the tangential mode and its linear dependency on the amplitude of the applied signal indicates that the tangential mode itself can serve as a micro rate table for in-site scale-factor calibration of gyroscopes²⁴⁻²⁶. Therefore, this technology provides the key building block for a BAW MEMS gyroscope with a built-in primary calibration stage.

4 Materials and Methods

Device fabrication Single crystal $[011]_c$ PMN-PT thin film samples (20 mm x 21 mm and approximately 6 μm -thick) are provided by iBule Photonics as attached to silicon substrate by means of epoxy application between the film and the silicon substrate. The schematic cross-section of the layer stack is depicted in Figure 2a. Fabrication of the resonators starts with wet etching of the PMN-PT film to get electrical access to the bottom electrode Pt layer as shown in Figure 2b, where the Pt layer acts as a natural etch stop in a 10 % HCl acid etch. The top electrode pattern along with the probe test pads and routing metal is deposited at the same lithographic step using liftoff. The top metal layer is evaporated as Ti/Au (10 nm/100 nm), where a 10 nm thick Ti layer is used as adhesion layer. In this step, the top electrode of the disk is defined slightly larger to ensure that even in the presence of misalignment of the resonator body to the top electrode, the entire resonator top surface will be covered by the top metal electrode. The resonator body is defined along with the side tethers in the same lithographic step eliminating possible anchor to resonator body misalignment that would cause more spurious modes or more pronounced mechanical loss through anchors. The anisotropic etching of the resonator body is realized using ion milling until the silicon layer underneath the film is fully exposed. Different from conventional ion milling, a new ‘CHISEL’ (CHanging Incident beam-angle for Sidewall Etching and Lapping) approach was developed and described in detail (Supplementary Note 1). The etching step is divided into cycles of varying ion beam incident angle making it possible to define vertical and residue-free side walls as depicted in Figure 2h.

Electrical and Optical Measurement Setup S_{11} measurements are performed using a ground-signal-ground (GSG) probe along with a network analyzer upon following a standard Short Open and Load (SOL) calibration protocol on an appropriate calibration substrate. Samples are wire-bonded to a fan-out PCB that allows coaxial connector connectivity for excitation for LDV measurements, which are performed using Polytec MSA 100-3D. Surface modifications were implemented using photoresist patterns to enable lateral displacement detection with enhanced diffuse scattering of the laser from the top electrode surface, which otherwise provided only specular re-

flection due to the smoothness of the top electrode surface.

Acknowledgements

This work was supported by DARPA MTO PRIGM-AIMS program agreement No: W911NF1820180. S.-G.L. and H.-S.P. were also supported by Korea Research Institute for Defense Technology Planning and Advancement (KRIT), F210001. The samples were fabricated in Birck Nanotechnology Center at Purdue University.

Conflict of interests

The authors declare no competing interests.

Author contributions

S.A.B, S.-G.L., and O.E. conceived the PMN-PT resonator design. S.-G.L. and H.-S.P. developed [011] PMN-PT-on-Silicon wafer-scale technology. O.E. performed design of experiments, microfabrication, electrical characterization and sample preparation for Laser Doppler Vibrometer (LDV) measurements. K.S. performed LDV measurements. S.A.B and S.L. supervised the project. O.E. and S.A.B. contributed to writing the manuscript with assistance from all other authors.

Additional information

See Supplementary Information for supporting content.

Data availability

Data Availability Statement: The code and data used to produce the plots within this work will be released on the repository Zenodo upon publication. Correspondence and requests for materials should be addressed to S.A.B.

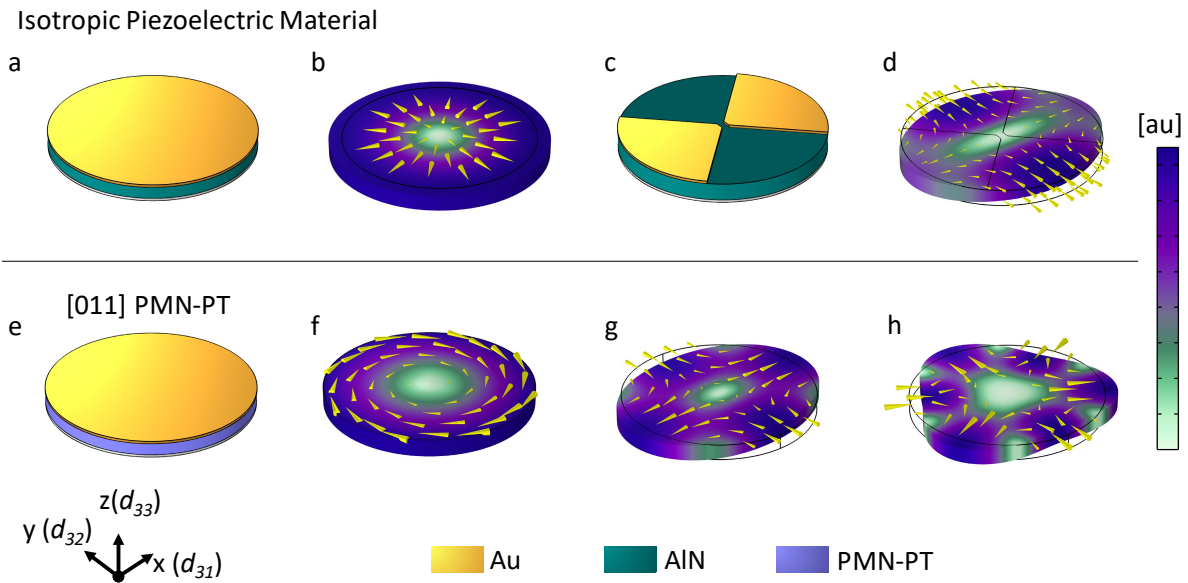


Figure 1: Schematic representation of disk resonator with single or split electrodes along with mode shapes of interest for conventional piezoMEMS materials (top row) and for PMN-PT (bottom row) Quiver plots (yellow cones that are proportional to the displacement magnitude) and color scale show displacement of each mode. **a** Disk resonator employing conventional piezoelectric material such as AlN with unpatterned top electrode **b** corresponding radial mode with exaggerated deformation (due to in-plane piezoelectric coefficients (d_{31} and d_{32}) having the same sign. **c** Disk resonator with segmented electrodes using the same in-plane piezoelectric coefficients with the same sign in order to excite n=2 wine-glass mode that is shown in **d**. The exaggerated deformation of strain profiles in x- and y-direction are opposite due to segmented electrode configuration. **e** Disk resonator employing [011] PMN-PT with a single electrode that is capable of exciting all the following mode shapes without the need for segmented electrodes due to in-plane piezoelectric anisotropy of the material: **f** Volume conserving tangential mode shape showing shear displacement **g** n=2 wine-glass mode, where the maximum displacement point is along x-axis **h** n=3 wine-glass mode.

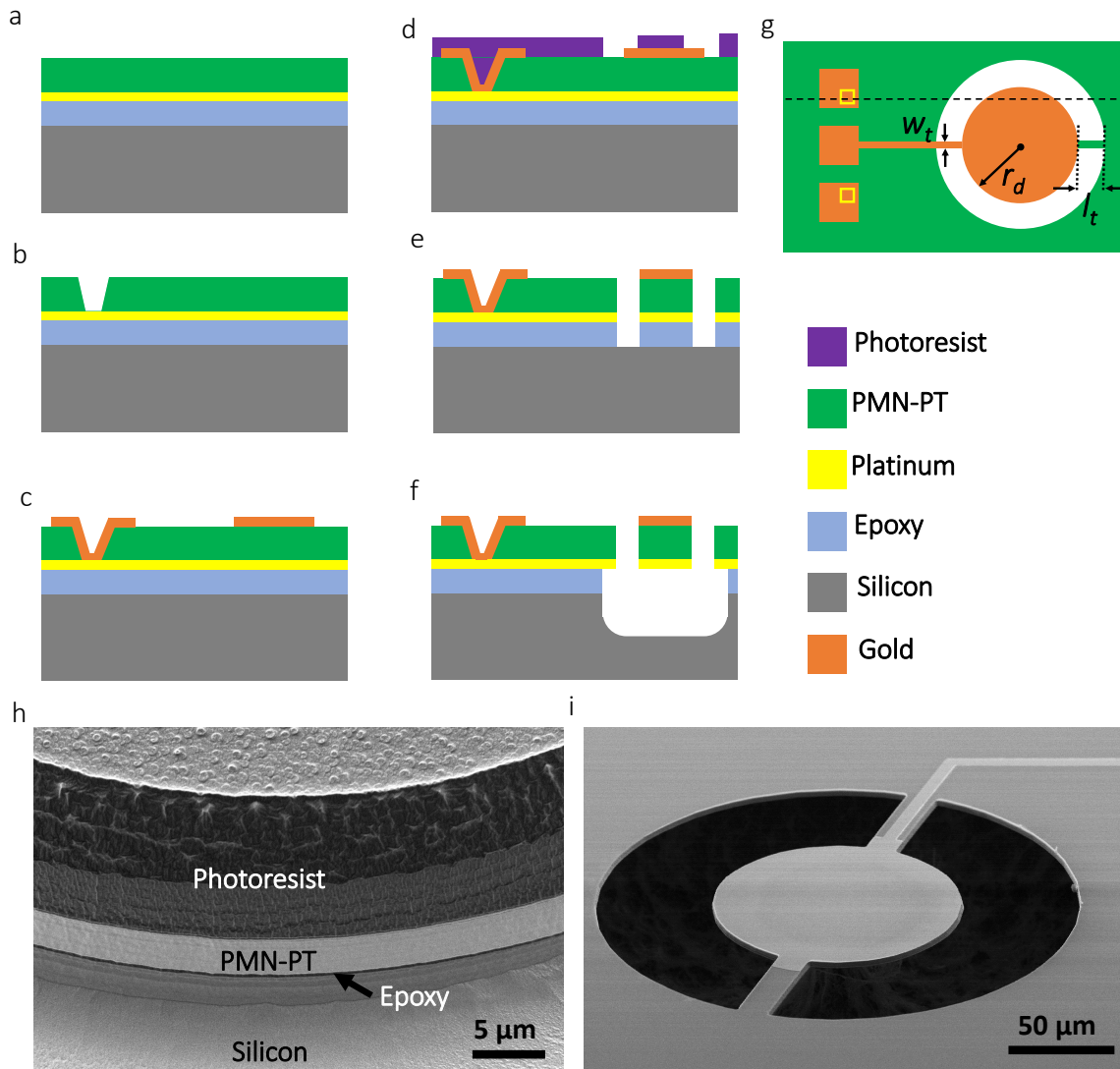


Figure 2: Fabrication process and SEM images **a** Initial layer stack schematic representation. **b** Wet etching of via openings for bottom electrode access. **c** Top metal deposition of Au layer **d** Lithographic patterning of etch gaps defining the resonator body smaller than the top electrode ensuring self-alignment. **e** Ion milling (CHISEL) of resonator body along with side tethers. **f** Releasing the resonator by XeF_2 etching of the silicon layer. **g** Schematic top view of the fabricated disk resonator and geometrical definitions **h** SEM image of the sidewall after CHISEL etch with annotated layers. Due to the cyclic changing incident ion beam, the photoresist layer seems to have different textures on the sidewall. **i** SEM image of the suspended device with two side tethers.

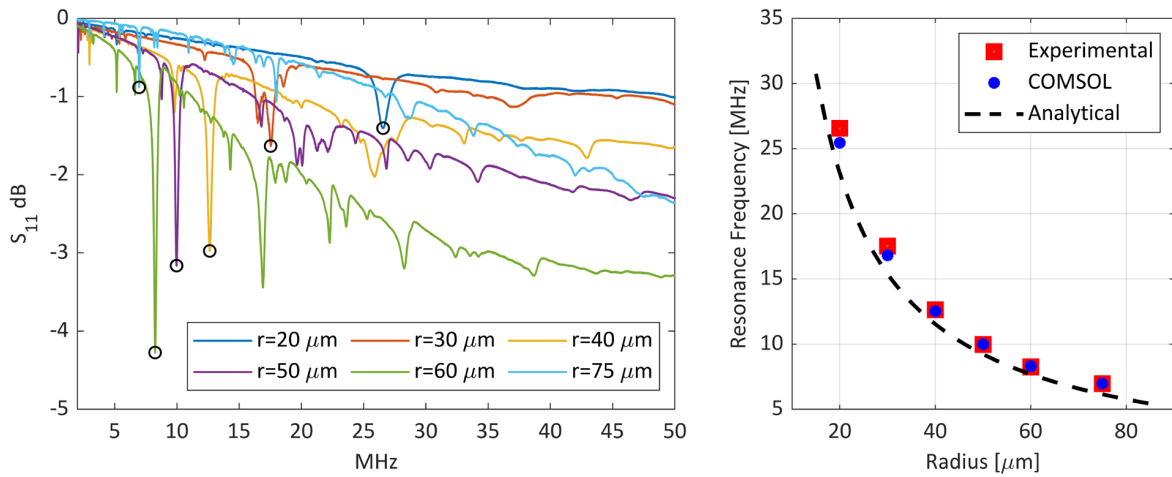


Figure 3: Electrical characterization results of disk resonators with varying radii with corresponding resonant frequencies **a** Overlaid plots of measured S_{11} data of disks with varying radii. The resonant dip that corresponds to WGM is encircled. **b** WGM frequency vs. disk radius, analytical, FEA, and measurement results compared. Note that the effect of anchors and tethers gets more drastic as the disk radius gets relatively smaller, hence the empirical results deviate more from the calculated values, especially for resonant frequency values estimated by analytical equations.

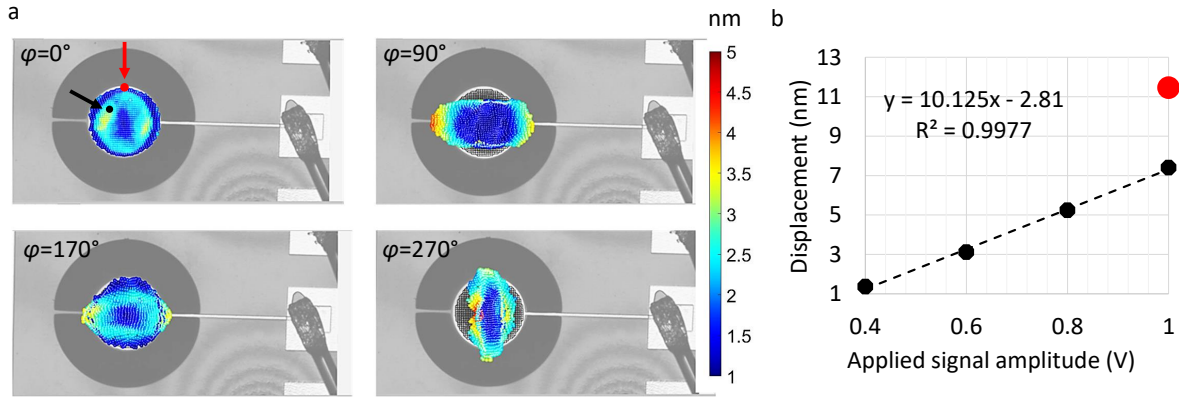


Figure 4: LDV results for n=2 wine-glass mode **a** LDV snapshots of a disk resonator with $r = 60\mu m$ radius shown at different phases of a single oscillation cycle at $\varphi = 0^\circ$, $\varphi = 90^\circ$, $\varphi = 170^\circ$, and $\varphi = 270^\circ$ **b** Displacement in the y-direction as a function of applied signal amplitude. Two distinct data points are plotted while maximum tip location is recorded (noted in red circle in the $\varphi = 0^\circ$ phase) while an inner point (noted by a black circle in the $\varphi = 0^\circ$ phase) displacement is recorded for various applied voltages. Linear fit to the displacement data along with the goodness of the fit is represented.

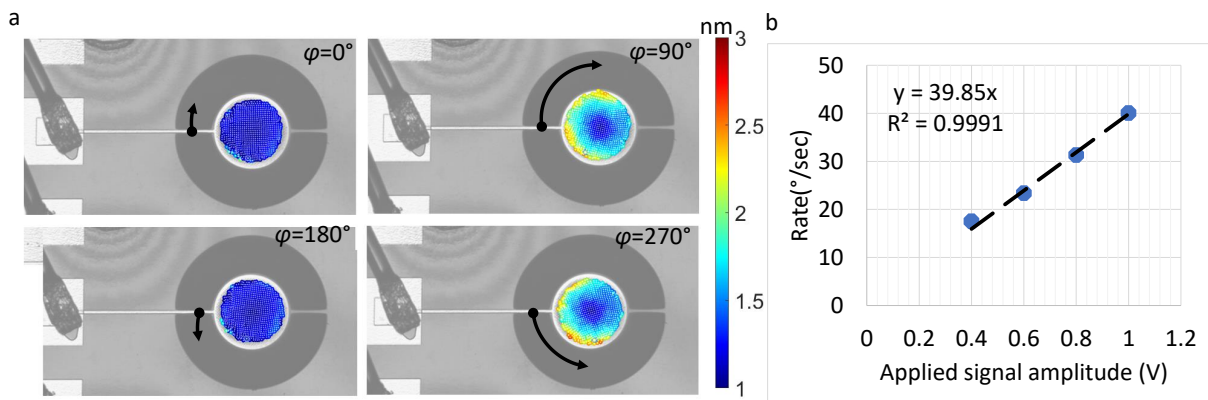


Figure 5: LDV results for tangential mode LDV snapshots of a disk resonator with $r = 60\mu m$ radius shown at different phases of a single oscillation cycle **a** LDV snapshots of disk resonator with $r = 60\mu m$ radius shown at different phases of a single oscillation cycle at $\varphi = 0^\circ$, $\varphi = 90^\circ$, $\varphi = 180^\circ$, $\varphi = 270^\circ$ **b** Rate of rotation is calculated from x- and y-displacement, and plotted with respect to applied signal amplitude. Linear fit of the data points is presented.

References

1. Onoe, M. Contour Vibrations of Isotropic Circular Plates. *The Journal of the Acoustical Society of America* **28**, 1158–1162 (1956). URL <http://asa.scitation.org/doi/10.1121/1.1908579>.
2. Abdelmoneum, M., Demirci, M. & Nguyen, C.-C. Stemless wine-glass-mode disk micromechanical resonators. In *The Sixteenth Annual International Conference on Micro Electro Mechanical Systems, 2003. MEMS-03 Kyoto. IEEE*, 698–701 (IEEE, 2003). URL <http://ieeexplore.ieee.org/document/1189845/>.
3. Pillai, G., Zope, A. A. & Li, S.-S. Piezoelectric-Based Support Transducer Design to Enable High-Performance Bulk Mode Resonators. *Journal of Microelectromechanical Systems* **28**, 4–13 (2019). URL <https://ieeexplore.ieee.org/document/8527654/>.
4. Elsayed, M. Y., Cicek, P.-V., Nabki, F. & El-Gamal, M. N. Bulk Mode Disk Resonator With Transverse Piezoelectric Actuation and Electrostatic Tuning. *Journal of Microelectromechanical Systems* **25**, 252–261 (2016). URL <http://ieeexplore.ieee.org/document/7397821/>.
5. Pulskamp, J. *et al.* Electrode-shaping for the excitation and detection of permitted arbitrary modes in arbitrary geometries in piezoelectric resonators. *IEEE Transactions on Ultrasonics, Ferroelectrics and Frequency Control* **59**, 1043–1060 (2012). URL <http://ieeexplore.ieee.org/document/6202429/>.
6. Matsumura, T. *et al.* Selective mode excitation of piezoelectric disk-type resonator by electrode pattern definition. In *2010 IEEE International Ultrasonics Symposium*, 979–982 (IEEE, 2010). URL <http://ieeexplore.ieee.org/document/5935435/>.
7. Wei, M., Avila, A., Rivera, I., Baghelani, M. & Wang, J. ZnO on nickel RF micromechanical resonators for monolithic wireless communication applications. *Journal of Micromechanics and Microengineering* **27**, 055006 (2017). URL <https://iopscience.iop.org/article/10.1088/1361-6439/aa635c>.
8. Hao, Z., Pourkamali, S. & Ayazi, F. VHF Single-Crystal Silicon Elliptic Bulk-Mode Capacitive Disk Resonators—Part I: Design and Modeling. *Journal of Microelectromechanical Systems* **13**, 1043–1053 (2004). URL <http://ieeexplore.ieee.org/document/1364064/>.
9. Serrano, D. E. *et al.* Substrate-decoupled, bulk-acoustic wave gyroscopes: Design and evaluation of next-generation environmentally robust devices. *Microsystems & Nanoengineering* **2**, 16015 (2016). URL <http://www.nature.com/articles/micronano201615>.
10. Ahn, C. H. *et al.* Mode-Matching of Wineglass Mode Disk Resonator Gyroscope in (100) Single Crystal Silicon. *Journal of Microelectromechanical Systems* **24**, 343–350 (2015). URL <http://ieeexplore.ieee.org/document/6844857/>.

11. Pourkamali, S., Hao, Z. & Ayazi, F. VHF Single Crystal Silicon Capacitive Elliptic Bulk-Mode Disk Resonators—Part II: Implementation and Characterization. *Journal of Microelectromechanical Systems* **13**, 1054–1062 (2004). URL <http://ieeexplore.ieee.org/document/1364065/>.
12. DeVoe, D. L. Piezoelectric thin film micromechanical beam resonators. *Sensors and Actuators A: Physical* **88**, 263–272 (2001). URL <https://linkinghub.elsevier.com/retrieve/pii/S0924424700005185>.
13. Dulmet, B., Ivan, M. E. & Ballandras, S. Electrostatic Generation of Bulk Acoustic Waves and Electrical Parameters of Si-MEMS Resonators. *IEEE Transactions on Ultrasonics, Ferroelectrics, and Frequency Control* **63**, 313–325 (2016). URL <http://ieeexplore.ieee.org/document/7342963/>.
14. Vukasin, G. D. *et al.* Anchor Design Affects Dominant Energy Loss Mechanism in a Lamé Mode MEM Resonator. *Journal of Microelectromechanical Systems* **29**, 860–866 (2020). URL <https://ieeexplore.ieee.org/document/9162109/>.
15. Kaajakari, V. *et al.* A 32.768 kHz MEMS Resonator with +/-20 ppm Tolerance in 0.9 mm x 0.6 mm Chip Scale Package. In *2019 Joint Conference of the IEEE International Frequency Control Symposium and European Frequency and Time Forum (EFTF/IFC)*, 48–51 (IEEE, 2019). URL <https://ieeexplore.ieee.org/document/8856015/>.
16. Sakr, M. M., El-Shafie, M. K. & Ragai, H. F. Analysis and Modeling of RF-MEMS Disk Resonator. In *2006 International Conference on MEMS, NANO, and Smart Systems*, 19–22 (IEEE, 2006). URL <http://ieeexplore.ieee.org/document/4155225/>.
17. Sun, E. & Cao, W. Relaxor-based ferroelectric single crystals: Growth, domain engineering, characterization and applications. *Progress in Materials Science* **65**, 124–210 (2014). URL <https://linkinghub.elsevier.com/retrieve/pii/S007964251400036X>.
18. Park, H. & Horsley, D. A. Single-Crystal PMN-PT MEMS Deformable Mirrors. *Journal of Microelectromechanical Systems* **20**, 1473–1482 (2011). URL <http://ieeexplore.ieee.org/document/6030900/>.
19. Liu, G., Jiang, W., Zhu, J. & Cao, W. Electromechanical properties and anisotropy of single- and multi-domain 0.72Pb(Mg 1/3 Nb 2/3)O 3 -0.28PbTiO 3 single crystals. *Applied Physics Letters* **99**, 162901 (2011). URL <http://aip.scitation.org/doi/10.1063/1.3652703>.
20. Wang, X. *et al.* E-field Control of the RKKY Interaction in FeCoB/Ru/FeCoB/PMN-PT (011) Multiferroic Heterostructures. *Advanced Materials* **30**, 1803612 (2018). URL <https://onlinelibrary.wiley.com/doi/10.1002/adma.201803612>.

21. Chen, X. *et al.* Electric field control of Néel spin–orbit torque in an antiferromagnet. *Nature Materials* **18**, 931–935 (2019). URL <http://www.nature.com/articles/s41563-019-0424-2>.
22. Hao, Z. & Ayazi, F. Support loss in micromechanical disk resonators. In *18th IEEE International Conference on Micro Electro Mechanical Systems, 2005. MEMS 2005.*, 137–141 (IEEE, 2005). URL <http://ieeexplore.ieee.org/document/1453886/>.
23. Hodjat-Shamami, M. & Ayazi, F. Eigenmode operation of piezoelectric resonant gyroscopes. *Microsystems & Nanoengineering* **6**, 108 (2020). URL <http://www.nature.com/articles/s41378-020-00204-3>.
24. Aktakka, E. E., Woo, J.-K. & Najafi, K. On-chip characterization of scale-factor of a MEMS gyroscope via a micro calibration platform. In *2017 IEEE International Symposium on Inertial Sensors and Systems (INERTIAL)*, 1–4 (IEEE, 2017). URL <http://ieeexplore.ieee.org/document/7935684/>.
25. Pinrod, V., Nadig, S., Ardanuc, S. & Lal, A. Piezoelectric micro dither stage calibration of 6-axis IMU. In *2016 IEEE 29th International Conference on Micro Electro Mechanical Systems (MEMS)*, vol. 2016-Febru, 990–993 (IEEE, 2016). URL <http://ieeexplore.ieee.org/document/7421799/>.
26. Pinrod, V., Nadig, S., Davaji, B. & Lal, A. 3-axis MEMS gyroscope calibration stage: Magnetic actuation enabled out-of-plane dither for piezoelectric in-plane calibration. In *2017 IEEE International Symposium on Inertial Sensors and Systems (INERTIAL)*, 136–139 (IEEE, 2017). URL <http://ieeexplore.ieee.org/document/7935692/>.